Ray-based Modeling of Unlicensed-Band mmWave Propagation inside a City Bus

Aleksei Ponomarenko-Timofeev[1], Aleksandr Ometov[1], and Olga Galinina[1]

Tampere University, Tampere, Finland
{aleksei.ponomarenko-timofeev,aleksandr.ometov,olga.galinina}@tuni.fi

Abstract. In the wake of recent hardware developments, augmented, mixed, and virtual reality applications – grouped under an umbrella term of eXtended reality (XR) – are believed to have a transformative effect on customer experience. Among many XR use cases, of particular interest are crowded commuting scenarios, in which passengers are involved in in-bus/in-train entertainment, e.g., high-quality video or 3D hologram streaming and AR/VR gaming. In the case of a city bus, the number of commuting users during the busy hours may exceed forty, and, hence, could pose far higher traffic demands than the existing microwave technologies can support. Consequently, the carrier candidate for XR hardware should be sought in the millimeter-wave (mmWave) spectrum; however, the use of mmWave cellular frequencies may appear impractical due to the severe attenuation or blockage by the modern metal coating of the glass. As a result, intra-vehicle deployment of unlicensed mmWave access points becomes the most promising solution for bandwidth-hungry XR devices. In this paper, we present the calibrated results of shooting-and-bouncing ray simulation at 60 GHz for the bus interior. We analyze the delay and angular spread, estimate the parameters of the Saleh-Valenzuela channel model, and draw important practical conclusions regarding the intra-vehicle propagation at 60 GHz.

Keywords: mmWave · SBR · Channel model · Wearables · Intra-vehicular.

1 Introduction

The rising consumer adoption of smart wearable devices is fueling the rapid growth of the wearable technology market, the revenues of which are expected to reach 30 billion by 2023 according to a CCS Insight forecast [1]. While a significant share of the heterogeneous wearables market is made up of gadgets with rather modest communication requirements (e.g., watches, wristbands, hearables, smart clothing, etc.), bandwidth-hungry devices dealing with video processing (head-mounted displays, smart glasses, and wearable cameras) are gaining increasing popularity as virtual, mixed, and augmented reality (AR/MR/VR) become mainstream.

Until recently, VR remained only a niche concept, its mass adoption severely hampered by the wired connections between the headset and external hardware, but this changed in 2018 by introducing a whole generation of untethered headsets. Although AR and MR devices have not been limited by the wires, their constraints come from

lower hardware capabilities that may impair the user experience; fortunately, the processing capacity can be enhanced today by, e.g., computational offloading to the network edge [2, 3].

In 2019, multiple hardware suppliers are already offering and shipping high-end wireless VR devices. The list of available products includes Oculus Quest (Project Santa Cruz), Lenovo Mirage Solo, HTC Vive Focus, DPVR M2 PRO, GenBasic Quad HD, and Xiaomi Mi VR. Some vendors have also supplemented older versions of headsets with wireless adapters, such as Intel's Wireless gigabit, TPCAST Wireless Adapter, and the HTC VIVE Wireless Adapter for same-brand devices, as well as the DisplayLink Wireless VR adapter. Just as important, the more affordable price (starting at $200 for some untethered headsets) could potentially serve as the main catalyst driving VR technology to the tipping point for the mass adoption [4].

In the wake of recent hardware developments, AR, MR, and VR applications – grouped under an umbrella term of *eXtended reality* (XR) [5, 6] – are believed to have a transformative effect on customer experience and, in general, the way people interact with real and digital worlds. In that regard, successful operation of XR devices imposes stringent communication requirements that include extremely high throughput to the processing unit [7] and ultra-low over-the-air latency as the total latency of the rendered image should be less than 15 ms to avoid motion sickness [8].

Beyond controversy, the growing density of demanding XR devices will result in increased traffic congestion, which would be impossible to resolve with the existing capacity of microwave networks. To ameliorate the situation, we may let the wireless XR devices take advantage of the high volume of spectrum available in millimeter-wave (mmWave) bands. The best candidate in the unlicensed mmWave frequency range is the 60 GHz band, where the channel access may be controlled by the IEEE 802.11ad (2012) or brand-new IEEE 802.11ay (expected to be ratified in 2020) protocols [9, 10].

Among several 802.11ad/ay use cases the IEEE 802.11 TGay Group adopted [11], of particular interest are crowded commuting scenarios, in which passengers are involved in in-bus/in-train entertainment, e.g., high-quality video or 3D hologram streaming and AR/VR gaming. To be able to predict the achievable performance of mmWave networks for these settings reliably, researchers need to develop a better understanding of the properties of the signal propagation in similar environments. The existing studies on intra-vehicular radio propagation are somewhat limited and address mainly the microwave spectrum: For example, the results of 2.4 GHz channel measurements and simulations inside a personal vehicle may be found in [12–14], while in [15–17], the authors build a propagation map for the airplane using ray-tracing simulation at 2.4 and 5.25 GHz. For the 28 GHz frequency, a study on the multiple-input–multiple-output (MIMO) performance in a subway tunnel is presented in [18].

In this paper, we make a first and important step toward the understanding of the structure of the 60 Hz channel for the intra-vehicle environment using an example of a city bus. We rely on the results of Wireless Insite, which is adopted by the community as a reliable ray-tracing simulator and based on the shooting-and-bouncing ray (SBR) method, and we also calibrate the obtained results with the outcomes of

our measurement campaign in [19]. Our main contribution lies in the analysis of the variation of delay and angular spreads in the radio channel and in estimating the parameters of the Saleh-Valenzuela channel model, which can be used in subsequent higher-level studies for synthesizing the channel impulse responses (CIRs).

The rest of the paper is organized as follows. Section 2 describes the scenario of interest and the calibration procedure. In Section 3, we provide selected numerical results related to the delay and angular spreads in our system. Section 4 presents the method of estimating parameters of the Saleh-Valenzuela statistical channel model, while our main conclusions are drawn in the last section.

2 Simulation scenario and calibration with measurements

In this work, we rely on simulation results obtained by the community-approved commercial tool, Wireless Insite [20], which exploits the shooting-and-bouncing ray (SBR) method. Here, we provide a detailed description of our intra-vehicle, city bus scenario represented by a 3D model, and also verify the choice of selected simulation parameters by calibrating with the outcomes of our measurement campaign in [19].

The 3D model of the bus is designed to match the bus interior and its dimensions (2.5 by 2.3 meters in cross-section and 12.5 meters length). The materials of individual model components and their electromagnetic properties are also adjusted according to the reference environment of the measurement campaign. Fig. 1 depicts the wireframe of our 3D model that replicates the actual bus interior and consists of four color-coded materials: particularly, window glass sections are colored green, metal parts (handles and railings) are black, interior body (plastic) is colored orange, and seats (velvet) are shown in blue. The corresponding material parameters, relative dielectric permittivity ϵ, conductivity σ, and thickness d, are given in Table 1.

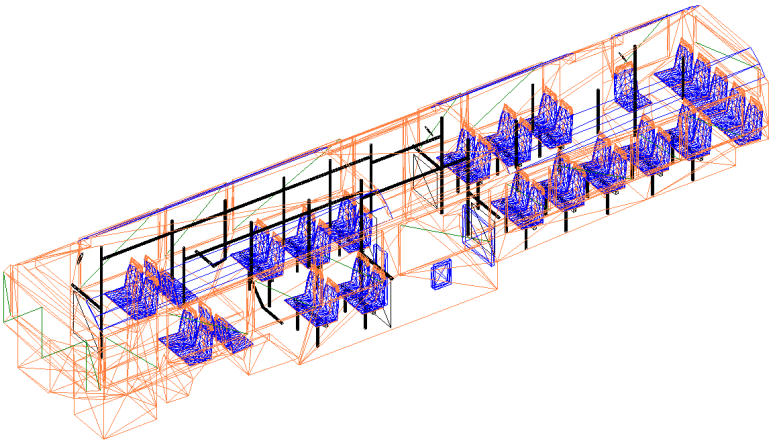

Fig. 1. Color-coded wireframe of the bus model: blue color corresponds to seat coating (velvet), green describes windows (glass), and red and black cover the bus body (plastic) and rails (metal).

Material	Conductivity, σ [S/m]	Permittivity, ϵ	Thickness, d [mm]
Glass (Window)	0.5674	6.27	7
Plastic (Body)	0.0586	1.50	3
Metal (Rails)	Perfect conductor		
Velvet (Seats)	Perfect absorber		

Table 1. Material properties

Further, we configure the transmitter/receiver deployment and antenna parameters so that they match those in the measurement campaign. In our scenario, receivers are placed on all seats at two levels for each position ("knee" and "headset") that are suggested in the reference paper and represent a wearable headset and a handheld device. The top-down view of our scenario, illustrating the locations of the receivers and the transmitter, is shown in Fig. 2. The core parameters are given in Table 2.

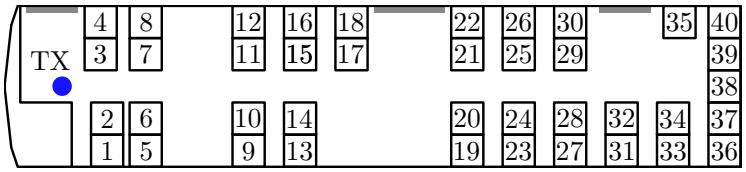

Fig. 2. Simulation scenario

Parameter	Transmitter	Receiver
Antenna type	Omnidirectional	
Half Power Beamwidth (HPBW)	40°	
Max. gain	0 [dBi]	
Polarization	Vertical	
Input power	0 [dBm]	—
Transmission line loss	0 [dBi]	—
Noise figure	—	3 [dBi]
Waveform	Sinusiod	
Center frequency	60 GHz	
Height	2.1 [m]	[0.7, 1.7] [m]

Table 2. Receiver/transmitter properties [19]

We calibrate our simulation environment with the measurement data in [19] by comparing the logarithmic path loss models that describe both sets of the path loss values. Using the SBR simulation data, we first estimate the coefficients of the distance-

dependent path loss function

$$L(d) = \alpha + 10\beta \log_{10}(d) + \chi(0, \sigma), \tag{1}$$

where α is the reference path loss value at the distance of 1 meter, β is the path loss exponent, which demonstrates how the signal attenuation evolves with the distance, and $\chi(0, \sigma)$ is a Gaussian random variable with standard deviation σ that corresponds to the channel fading.

The comparison of the two path loss models is illustrated in Fig. 3. The coefficients obtained by regression are the following: $\alpha_{sim} = 88.66$ dB, $\alpha_{meas} = 85.28$ dB, $\beta_{sim} = 1.06$, $\beta_{meas} = 1.74$, $\sigma_{sim} = 2.54$, and $\sigma_{meas} = 6.93$. For our data set, α differs from that of the reference path loss model only by 3 dB; however, standard deviation σ_{meas} and exponent β_{meas} exceed the respective values obtained through the simulation, which can be explained by the fact that not every small detail is included in the model to optimize the simulation time.

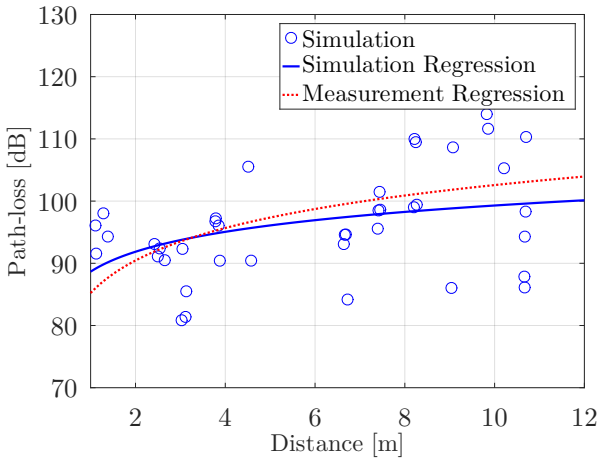

Fig. 3. Calibration results: comparison of the simulation path loss data (blue color) and the reference logarithmic path loss model that is based on measurements (dotted red curve).

In addition, we note that the parameters of the X3D (extensible 3D) engine performing the SBR simulation are configured to record three reflections, one diffraction, and transmission per path. In total, the engine records up to 250 propagation paths with a noise floor of -140 dBm. Ray spacing for the geometry engine is set to 0.2°. This choice of the engine parameters allows us to maintain the required precision while keeping the simulation times under eight hours for Intel Core 2 Quad CPU (model Q9500), 8 GB of RAM, nVidia GTX 550 Ti GPU, and 200 GB HDD (WD Blue at 5400 RPM).

3 RMS delay and angular spread

In this section, we study the angular and delay spreads obtained from the simulation data. This analysis may help to estimate the coherence bandwidth and also explore, whether one may potentially mitigate the inter-symbol interference (ISI) by adjusting an antenna array pattern.

3.1 Delay spread analysis

One of the key metrics for wireless channels is the coherence bandwidth that allows estimating the frequencies, over which the channel has a flat frequency response. The information on the expected channel coherence bandwidth can be used in designing hardware for the communication systems. Specifically, it may help the engineer in estimating the impact of ISI and the complexity of an equalizer. The coherence bandwidth can be calculated as an inverse of root-mean-square (RMS) delay spread σ_τ, which is defined as

$$\sigma_\tau = \sqrt{\frac{\sum_{i=0}^{N} p_i \cdot (\tau_i - \hat{\tau})^2}{\sum_{i=0}^{N} p_i}}, \tag{2}$$

where N is the total number of propagation paths, p_i is power delivered over path i, τ_i is the arrival time of path i, and $\hat{\tau}$ is the earliest arrival time in the CIR.

We calculate the delay spread for both positions (higher "headset" and lower "knee") of the receivers. While the difference between the two positions is relatively small in terms of the distance to the receiver, no line-of-sight (LOS) path exists in the case of the "knee" level. To obtain the data set required for analyzing the delay (and also angular) spread, we cover the entire plane by receivers at the "waist" (pocket) level, which would not be possible to accomplish during a measurement campaign.

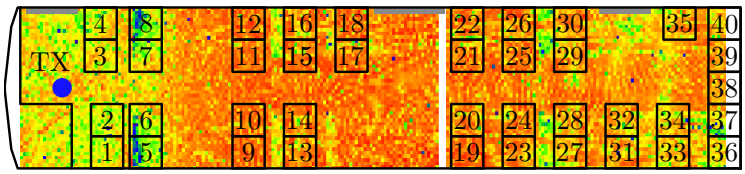

Fig. 4. Received power heat-map

For "waist"-level positions, we observe that the delay spread decreases with the distance between the transmitter and receiver, which is caused primarily by the fact that at low distances, the radiation pattern of the antenna impedes the communication over LOS links and results in multiple NLOS components. Also, since the root mean square (RMS) delay spread is a weighted variance of the arrival time (with the component power being the weight), even if a weak LOS component is present, it will have the weight comparable to those of the NLOS components.

In Fig. 5, we observe that at short ranges, the delay spread is higher due to the antenna patterns of both receiver and transmitter; irregularities in the environment explain a small rise at a range of 7–9 meters. Moreover, the positions at "knee" level have lower delay spread, which may have been caused by the following two factors. First, the range of paths, over which signal may propagate, is limited since reflections can mainly occur either from the windows or the floor. Another important factor is the presence of a perfect absorber (velvet seats), which also reduces the number of propagation paths and ultimately leads to the narrower range of the path length and, hence, a decrease in the delay spread.

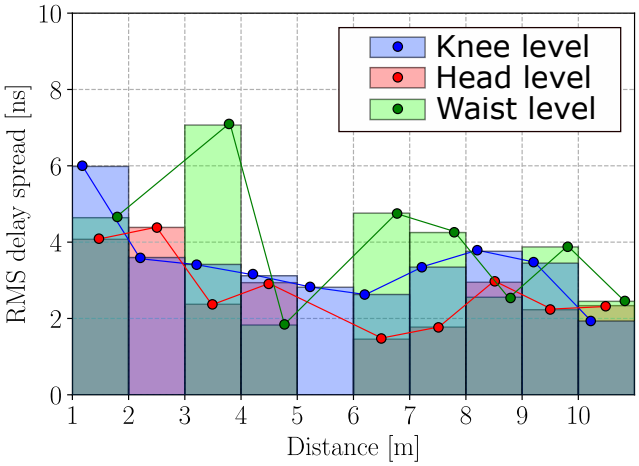

Fig. 5. Delay spread vs. distance

3.2 Angular spread analysis

Further, we study the root mean square (RMS) angular spread, which may serve in estimating the coherence distance of a channel that, in turn, helps to determine, whether specific hardware can exploit spatial diversity.

The histogram of RMS angular spread in Fig. 6 shows that at short ranges, the angular spread is smaller for the "headset" level. Coupled with the previous result, it may indicate that filtering undesired MPCs by tuning the receive antenna pattern might be unfeasible. For the "knee" level, however, the angular spread mostly maintains relatively consistent values. For all locations at the "waist" level, the angular spread increases with the distance since the number of interactions (reflection, diffraction) increases. However, due to the blockage by the seats (even at short ranges), the change in the angular spread is not as pronounced as for the "head" level.

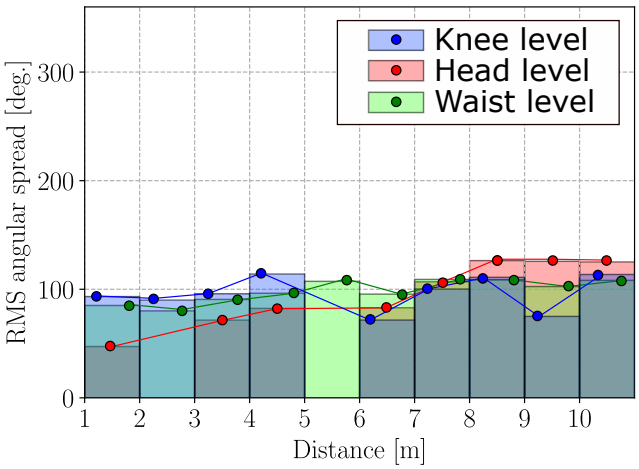

Fig. 6. Angular spread vs. distance

4 Saleh-Valenzuela statistical model

In this section, we analyze the CIRs produced by the simulation and estimate the parameters of Saleh-Valenzuela clustering model [21]. The Saleh-Valenzuela model is a statistical multipath model, where the received rays arrive in clusters so that the clusters and the rays arrivals form a Poisson process and amplitudes decay exponentially. The model generates artificial CIRs corresponding to specific environment type and defines the CIR through the Dirac delta function as follows

$$h(t) = \sum_{j=0}^{\infty} \sum_{k=0}^{\infty} \beta_{jk} e^{i\theta_{jk}} \delta(t - T_j - \tau_{jk}), \tag{3}$$

where β_{jk} and θ_{jk} are the gain and the phase of ray k in cluster j, T_j is the arrival time of cluster j and τ_{jk} is the arrival time of ray k in this cluster. While the phase θ is a uniform independent random variable within a range of $(0, 2\pi)$, gain β_{jk} is assumed to be a Rayleigh random variable. Mean square values of β_{jk} can be found as

$$\overline{\beta^2(T_j, \tau_{jk})} = \overline{\beta^2(0,0)} e^{-T_j/\Gamma} e^{-\tau_{jk}/\gamma}, \tag{4}$$

where $\overline{\beta^2(0,0)}$ is the first ray power in the first cluster [22], Γ and γ are the power decay constants for clusters and rays, correspondingly. Inter-arrival times for clusters and rays T_j and τ_{jk} are defined by independent exponential probability density functions [22] as

$$p(T_j|T_{j-1}) = \Lambda \exp\big[-\Lambda(T_j - T_{j-1})\big], \tag{5}$$

$$p(\tau_{jk}|\tau_{j,k-1}) = \lambda \exp\big[-\lambda(\tau_{jk} - \tau_{j,k-1})\big], \tag{6}$$

where Λ and λ are the cluster and ray arrival rates. In Fig. 7, we schematically illustrate parameters $\lambda, \Lambda, \gamma, \Gamma, \beta(0,0)$ of the model, binding them to the physical aspect.

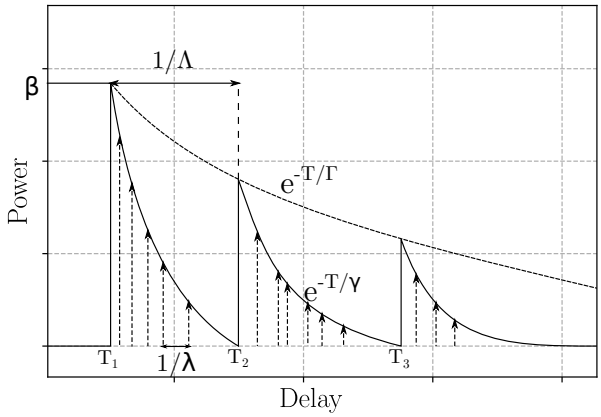

Fig. 7. Example of a synthetic CIR produced by the Saleh-Valenzuela model

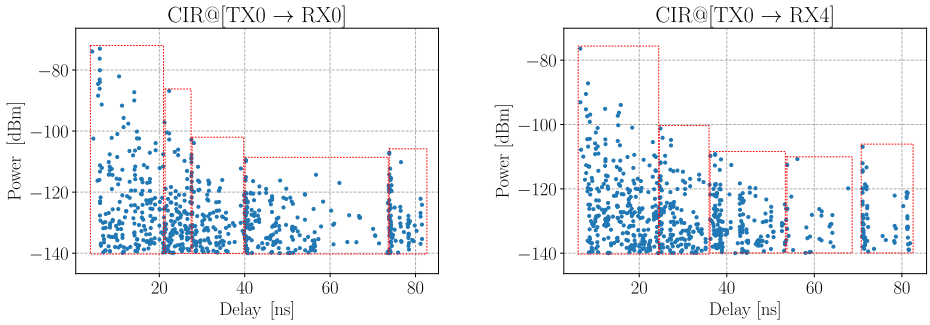

(a) RX0 (b) RX4

Fig. 8. Channel impulse response with identified clusters for receiver locations "0" and "4"

Following the methodology in [22], we use visual observation to analyze the CIRs and identify clusters. Selected examples of CIRs with identified clusters for several receiver locations are shown in Fig. 8–11 (see Fig. 2 for reference locations).

We begin with Fig. 8 illustrating the power delay profile (PDP), measured at two seats located closer to the transmitter, and corresponding identified ray clusters. At short ranges, we notice that the amplitude of the last clusters in the shown CIRs exceeds that of the preceding one, which corresponds to a path that experiences two reflections (from the windshield and the rear window) at nearly 90° angle and caused by the antenna patterns with a narrow mainlobe.

In Fig. 9, we observe more sparse CIR due to the increasing distance between the receiver and the transmitter. Components that are reflected from both windshield and rear window disappear in Fig. 9(b) as the corresponding paths become blocked at this position and further. Interestingly, in Fig. 10, the number of clusters decreases, which is due to the elements of the bus interior, which block or attenuate some of

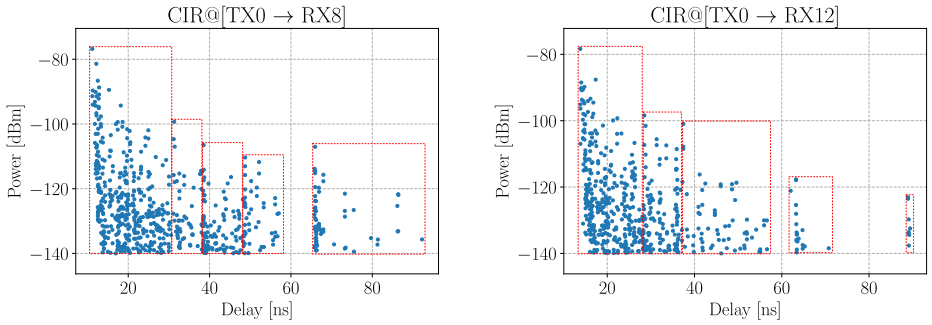

(a) RX8 (b) RX12

Fig. 9. Channel impulse response with identified clusters for receiver locations "8" and "12"

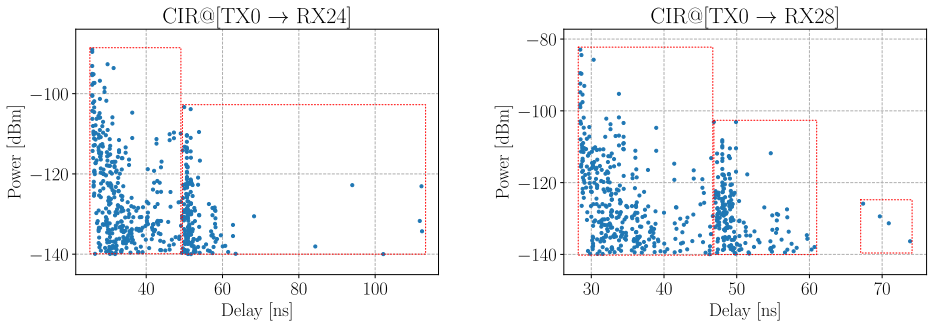

(a) RX24 (b) RX28

Fig. 10. Channel impulse response with identified clusters for locations "24" and "28"

the clusters that are present in previous figures. Further, in Fig. 11, we observe that clusters merge, and the components are located within the first two clusters, which is caused by the fact that all propagation paths with more substantial delays are attenuated (based on the delay values, the average path length is around 13 meters, which corresponds to the length of the bus).

Finally, based on these and other identified clusters, we can estimate the parameters of the Saleh-Valenzuela model as it has been done, e.g., in [22] or other similar literature on channel modeling. To calculate the ray arrival rate λ, we consider only dominant MPC components and omit nearby low-powered components. The resulting parameters of the statistical cluster model for our data set are $\Lambda = 0.29$, $\lambda = 3.45$, $\gamma = 0.67$, and $\Gamma = 0.85$. For convenience, all parameters are collected in Table 3.

5 Conclusions and discussion

In this paper, we study the intra-vehicular propagation at 60 GHz using the ray-based simulation of a scenario that mimics a realistic interior of a typical city bus. We construct a highly detailed 3D model of the bus environment, calibrate the simulation

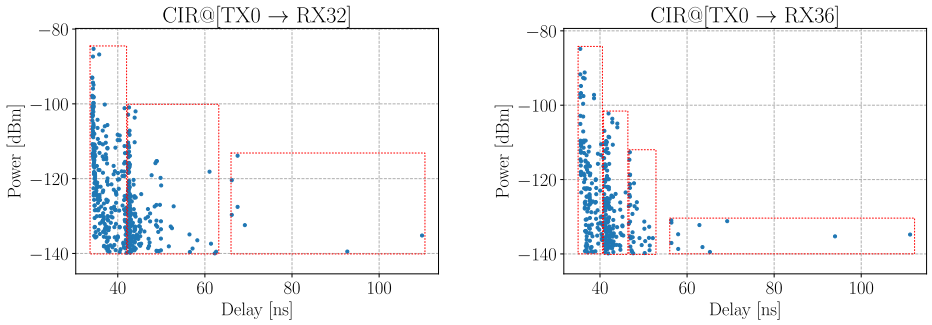

(a) RX32 (b) RX36

Fig. 11. Channel impulse response with identified clusters for locations "32" and "36"

Cluster arrival rate, Λ	Ray arrival rate, λ	Cluster power decay, Γ	Ray power decay, γ
0.29 ns^{-1}	3.45 ns^{-1}	0.85 ns	0.67 ns

Table 3. Parameters of the Saleh-Valenzuela model for our intra-vehicle scenario (city bus)

scenario with our prior results obtained during a measurement campaign, and adjust the parameters, striking a balance between the simulation time and appropriate accuracy. Using the obtained simulation data, we extract CIRs and analyze the delay and angular spreads, which might prove useful for hardware engineers when estimating the required complexity of equalizers at the receiver based on the operational bandwidth.

We place the receivers at three different levels: the "knee" and "headset" levels on every seat, as well as the "waist" level covering the entire bus space. The delay spread at the "knee" level appears to be lower than that at the "headset" level, which translates to the narrower coherence bandwidth for "headsets". Hence, such aspects as ISI will be more pronounced at the "headset" level than for the "knee" locations. Moreover, the delay spread decreases with the growing distance due to the antenna directivity pattern; a sudden increase at 7 to 10 meters is caused by the presence of the second exit in the rear part of the bus. Interestingly, the presence of exit and railings form a notable irregularity in the environment as we demonstrate on the power heatmap. Further, for the higher angular spread, it may be possible to isolate the ISI by configuring antenna pattern at receiver, which, however, might become infeasible for the "headset" level, if the antenna arrays in the respective hardware are simplistic.

Finally, we analyze a clustering structure of the power delay profile and derive statistical characteristics of the channel using the Saleh-Valenzuela cluster model. The obtained statistical multipath model can be directly implemented in link- and system-level studies to reproduce the structure of the 60 GHz channel in large intra-vehicle scenarios.

References

1. CCSInsight, "Optimistic outlook for wearables." https://www.ccsinsight.com/press/company-news/optimistic-outlook-for-wearables/, March 2019. Accessed in July 2019.
2. M. Satyanarayanan, "The Emergence of Edge Computing," *Computer*, vol. 50, no. 1, pp. 30–39, 2017.
3. A. Ometov, D. Kozyrev, V. Rykov, S. Andreev, Y. Gaidamaka, and Y. Koucheryavy, "Reliability-Centric Analysis of Offloaded Computation in Cooperative Wearable Applications," *Wireless Communications and Mobile Computing*, 2017.
4. Aniwaa Pte. Ltd., "The best all-in-one VR headsers of 2019." https://www.aniwaa.com/best-of/vr-ar/best-standalone-vr-headset/, June 2019.
5. Forbes Media LLC, "Preparing Enterprises For The Extended Reality Explosion." https://www.forbes.com/sites/joemckendrick/2019/05/21/preparing-enterprises-for-the-extended-reality-explosion/\#570d20fd24d9, May 2019.
6. Qualcomm Technologies, Inc., "The Mobile Future of eXtended Reality (XR)." https://www.qualcomm.com/media/documents/files/the-mobile-future-of-extended-reality-xr.pdf, October 2018.
7. O. Abari, D. Bharadia, A. Duffield, and D. Katabi, "Cutting the Cord in Virtual Reality," in *Proc. of the 15th ACM Workshop on Hot Topics in Networks*, pp. 162–168, ACM, 2016.
8. K. Doppler, E. Torkildson, and J. Bouwen, "On wireless networks for the era of mixed reality," in *2017 European Conference on Networks and Communications (EuCNC)*, pp. 1–5, IEEE, 2017.
9. IEEE 802.11 Working Group, "Wireless LAN Medium Access Control (MAC) and Physical Layer (PHY) Specifications. Amendment 3: Enhancements for Very High Throughput in the 60 GHz Band," 2012.
10. Y. Ghasempour, C. R. da Silva, C. Cordeiro, and E. W. Knightly, "IEEE 802.11 ay: Next-generation 60 GHz communication for 100 Gb/s Wi-Fi," *IEEE Communications Magazine*, vol. 55, no. 12, pp. 186–192, 2017.
11. IEEE 802.11 Working Group, "IEEE 802.11 TGay Use Cases," 2015.
12. T. R. Rao, D. Balachander, P. Sathish, and N. Tiwari, "Intra-Vehicular RF Propagation Measurements at UHF for Wireless Sensor Networks," in *Proc. of International Conference on Recent Advances in Computing and Software Systems*, pp. 214–218, IEEE, 2012.
13. C. A. Costa, H. Gao, T. Le Polain, R. Van Dommele, B. Smolders, M. Dheans, and P. Baltus, "Damper-to-Damper Path Loss Characterization for Intra-Vehicular Wireless Sensor Networks," in *Proc. of 47th European Microwave Conference (EuMC)*, pp. 1341–1344, IEEE, 2017.
14. C. U. Bas and S. C. Ergen, "Ultra-Wideband Channel Model for Intra-Vehicular Wireless Sensor Networks Beneath the Chassis: From Statistical Model to Simulations," *IEEE Transactions on Vehicular Technology*, vol. 62, no. 1, pp. 14–25, 2012.
15. K. Chetcuti, C. J. Debono, R. A. Farrugia, and S. Bruillot, "Wireless Propagation Modelling inside a Business Jet," in *Proc. of IEEE EUROCON 2009*, pp. 1644–1649, IEEE, 2009.
16. C. J. Debono, R. A. Farrugia, and K. Chetcuti, "Modelling of the Wireless Propagation Characteristics inside Aircraft," in *Aerospace Technologies Advancements*, IntechOpen, 2010.

17. R. DeHaan, *Ray-tracing Techniques and The Simulation of Large-Scale In-Flight Wi-Fi Signal Propagation*. PhD thesis, Baylor University, 2018.
18. Y. Jiang, G. Zheng, X. Yin, A. Saleem, and B. Ai, "Performance Study of Millimetre-Wave MIMO Channel in Subway Tunnel Using Directional Antennas," *IET Microwaves, Antennas & Propagation*, vol. 12, no. 5, pp. 833–839, 2017.
19. V. Semkin, A. Ponomarenko-Timofeev, A. Karttunen, O. Galinina, S. Andreev, and Y. Koucheryavy, "Path Loss Characterization for Intra-Vehicle Wearable Deployments at 60 GHz," *arXiv preprint arXiv:1902.01949*, 2019.
20. P. Mededović, M. Veletić, and Ž. Blagojević, "Wireless Insite Software Verification via Analysis and Comparison of Simulation and Measurement Results," in *Proc. of the 35th International Convention MIPRO*, pp. 776–781, IEEE, 2012.
21. A. A. Saleh and R. Valenzuela, "A statistical model for indoor multipath propagation," *IEEE Journal on selected areas in communications*, vol. 5, no. 2, pp. 128–137, 1987.
22. Q. H. Spencer, B. D. Jeffs, M. A. Jensen, and A. L. Swindlehurst, "Modeling the statistical time and angle of arrival characteristics of an indoor multipath channel," *IEEE Journal on Selected areas in communications*, vol. 18, no. 3, pp. 347–360, 2000.